

Fully Dense UNet for 2D Sparse Photoacoustic Tomography Artifact Removal

Steven Guan, Amir Khan, Siddhartha Sikdar, and Parag V. Chitnis

Abstract— Photoacoustic imaging is an emerging imaging modality that is based upon the photoacoustic effect. In photoacoustic tomography (PAT), the induced acoustic pressure waves are measured by an array of detectors and used to reconstruct an image of the initial pressure distribution. A common challenge faced in PAT is that the measured acoustic waves can only be sparsely sampled. Reconstructing sparsely sampled data using standard methods results in severe artifacts that obscure information within the image. We propose a novel convolutional neural network (CNN) architecture termed Fully Dense UNet (FD-UNet) for removing artifacts from 2D PAT images reconstructed from sparse data and compare the proposed CNN with the standard UNet in terms of reconstructed image quality.

Index Terms—Image reconstruction, image restoration, tomography, photoacoustic imaging, biomedical imaging

I. INTRODUCTION

PHOTOACOUSTIC imaging (PAI) is an emerging imaging modality based upon the photoacoustic effect, in which a medium absorbing electromagnetic waves results in the generation of acoustic waves [1]–[3]. PAI benefits from the advantages of optical and ultrasound imaging without suffering from the major drawbacks found in each technique alone [4]. It combines the high contrast of optical imaging with the resolution and penetration depth of ultrasound imaging. PAI is performed by illuminating a semi-transparent sample with short laser pulses. In photoacoustic tomography (PAT), the induced acoustic pressure waves are measured by an array of detectors that are commonly arranged in a spherical, cylindrical, or planar geometry surrounding the sample [5]. The goal in PAT image reconstruction is to recover the initial pressure distribution using the measured pressure data. This task is a well-studied inverse problem that can be solved using methods such as filtered back projection [6], Fourier methods [7], [8], and time reversal (TR) [9]–[11]. While each method has its own advantages and challenges, TR is a robust method considered to be the least restrictive because it works well for any arbitrary detection geometry and also for heterogenous medias [12].

A common challenge faced in PAT is that the measured acoustic waves can only be sparsely sampled in the spatial

dimension. Each discrete spatial measurement requires its own detector, and it may be infeasible to build an imaging system with a sufficiently large number of detectors due to practical and physical limitations [13]–[15]. Reconstructing sparsely sampled data using standard methods results in severe artifacts that obscure information within the image. The artifacts can be reduced by using iterative methods that incorporate prior knowledge such as smoothness, sparsity, and total variation constraints [15]–[18]. However, iterative methods are typically time consuming because the optimization process requires repeated evaluations of the forward and adjoint operators and selection of appropriate constraints.

Deep learning is an emerging research area, in which specialized artificial neural networks are used for pattern recognition and machine learning tasks [19]. In particular, convolutional neural networks (CNN) are widely used for imaging tasks such as classification and segmentation [20]–[23]. For biomedical image reconstruction, there are two different approaches reported in literature that utilizes deep learning. In the first approach, the raw measurement data is initially reconstructed into an image using a simple inversion step. The image is then post-processed using a CNN to remove artifacts and improve its overall quality. This approach has been successfully applied to CT, MRI, and PAT [24]–[27]. Antholzer et al showed that the UNet CNN architecture can recover images with comparable quality to those reconstructed using classical iterative methods for sparse 2D PAT [24]. In the second approach, a CNN is used to learn appropriate prior constraints to be used in an iterative reconstruction method [28]. Hauptmann, et al successfully applied this second approach for limited-view photoacoustic tomography and showed that prior constraints learned by the CNN enables for faster and higher quality image reconstructions. In general, deep learning-based approaches allows for faster image reconstruction with comparable image quality to state-of-the-art reconstruction methods. Although training the network is computationally intensive, a forward pass through the trained network is relatively inexpensive.

In our work, we follow the first approach in using the CNN as a post-processing tool for removing artifacts and improving image quality. We propose a novel CNN architecture termed Fully Dense UNet (FD-UNet) for removing artifacts from 2D

[§] Guan is with the Bioengineering Department, George Mason University, Fairfax, VA 22031 USA. (e-mail: sguan2@gmu.edu) and The MITRE Corporation, McLean, VA, 22102 (e-mail: sguan@mitre.org). The author's affiliation with The MITRE Corporation is provided for identification purposes only and is not intended to convey or imply MITRE's concurrence with, or support for, the positions, opinions or viewpoints expressed by the author.

Approved for Public Release; Distribution Unlimited. Case Number 18-2222. ©2018 The MITRE Corporation. All Rights Reserved.

A. Khan, and P. Chitnis, S. Sikdar are with the Bioengineering Department, George Mason University, Fairfax, VA 22031 USA. (e-mail: akhan50@gmu.edu, pchitnis@gmu.edu, and ssikdar@gmu.edu).

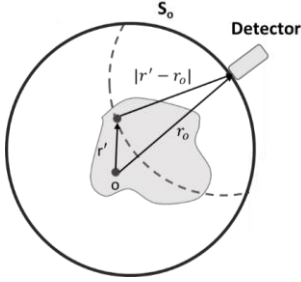


Fig. 1. Detector at position r_o on the boundary S_o measures the acoustic pressure emitted from a source located at r' . Adapted from [5].

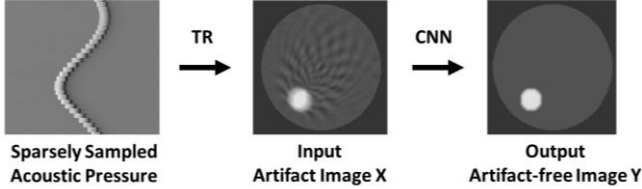


Fig. 2. Deep learning framework for 2D PAT image reconstruction. The sparsely sampled acoustic pressure is reconstructed into an image containing artifacts using time reversal. A CNN is applied to the artifact image X to obtain an approximately artifact free image Y .

PAT images reconstructed from sparse data. The FD-UNet incorporates dense connectivity into both the contracting and expanding paths of the UNet. Dense connectivity mitigates learning redundant features, enhances information flow, and reduces the number of parameters required to achieve similar or better performance compared to traditional CNNs [21], [29], [30]. Having a more compact CNN requires less computation and results in faster image reconstruction. In this work, we compare the proposed FD-UNet to its standard counterpart in terms of image reconstruction quality.

A. Related Work

The UNet has been previously demonstrated to perform comparatively well to iterative methods for reconstructing CT and PAT images from sparse data [24]–[28]. Inspired by the work of Antholzer et al, we are also training and testing our CNN using synthetically generated data. We build upon their work by incorporating dense connectivity into the UNet, use more complex phantoms, and testing the CNN’s performance under varying levels of sampling sparsity. In addition to dense connectivity, our UNet implementation applies batch normalization to accelerate the training process [31], [32].

Li Et al. has previously proposed a hybrid densely connected UNet for liver and tumor segmentation from CT volumes [30]. In their work, they show that including dense connectivity improves the performance of the 2D UNet. While the FD-UNet similarly incorporates dense connectivity, there are key differences between the two CNN implementations. In the FD-UNet, dense connectivity is incorporated into both the expanding and contracting paths of the UNet, which enables the benefits of dense connectivity to be leveraged throughout the entire network. Also, there is no compression of features-maps learned by each dense block prior to each max-pooling operation. This promotes feature reuse and reduces learning

redundant features since each subsequent level of the UNet has access to max-pooled versions of all previously learned feature-maps. Finally, the dense block growth rate is updated accordingly at each level of the FD-UNet. This improves computational efficiency by ensuring all dense blocks have the same number of convolution layers. To the best of our knowledge, this is the first work applying the UNet with dense connectivity for removing artifacts in sparse PAT image reconstruction.

II. METHODS

In PAT, the sample is irradiated by a short laser pulse $\delta(t)$ which leads to the generation of an initial acoustic pressure $p_o(\mathbf{r})$ via thermo-elastic expansion [3]. Given the initial pressure, the acoustic pressure wave $p(\mathbf{r}, t)$ at position \mathbf{r} and time t satisfies the following wave equation.

$$\left(\nabla^2 - \frac{1}{c^2} \frac{\partial^2}{\partial t^2}\right) p(\mathbf{r}, t) = -p_o(\mathbf{r}) \frac{d\delta(t)}{dt} \quad (1)$$

Detectors at position \mathbf{r}_o are located on a measurement surface S_o that encloses the sample as seen in Fig. 1. Each detector along the surface measures a time-dependent signal of the emitted pressure wave over a period of time T . If a sufficiently large number of detectors are used then standard reconstruction techniques would yield an essentially artifact-free image [13]. In the 2D case, an image $X \in \mathbb{R}^{d \times d}$ would require $M \geq \pi d$ detectors to satisfy Shannon’s sampling theory. However, in most practical applications there are $M \ll \pi d$ detectors leading to a reconstructed image containing artifacts.

A. Deep Learning Framework

As shown in Fig. 2., the sparsely sampled acoustic pressure is initially reconstructed using TR into an image X containing artifacts. The CNN is then applied to correct the undersampling artifacts in image X to obtain an approximately artifact-free image Y . This task can be formulated as a supervised learning problem, in which the goal is to learn a restoration function that maps an input image X to the desired output image Y [24]. Other reconstruction methods can be used in place of TR such as filtered back projection.

B. FD-UNet

The FD-UNet is based on the UNet architecture which is comprised of a contracting and expanding path [20], [26], [33]. As seen in Fig. 3., the image undergoes a multilevel decomposition via max-pooling followed by an upsampling process via deconvolution. This enables the CNN to efficiently learn local and global image features at different spatial scales [34]. Dense blocks with a growth rate, k are used to learn the desired number of feature-maps, f . The growth rate is updated at each layer so that all dense blocks have the same number of convolutional layers. Concatenation connections are added between the contracting and expanding path, which allows the CNN to use finer resolution features learned earlier for

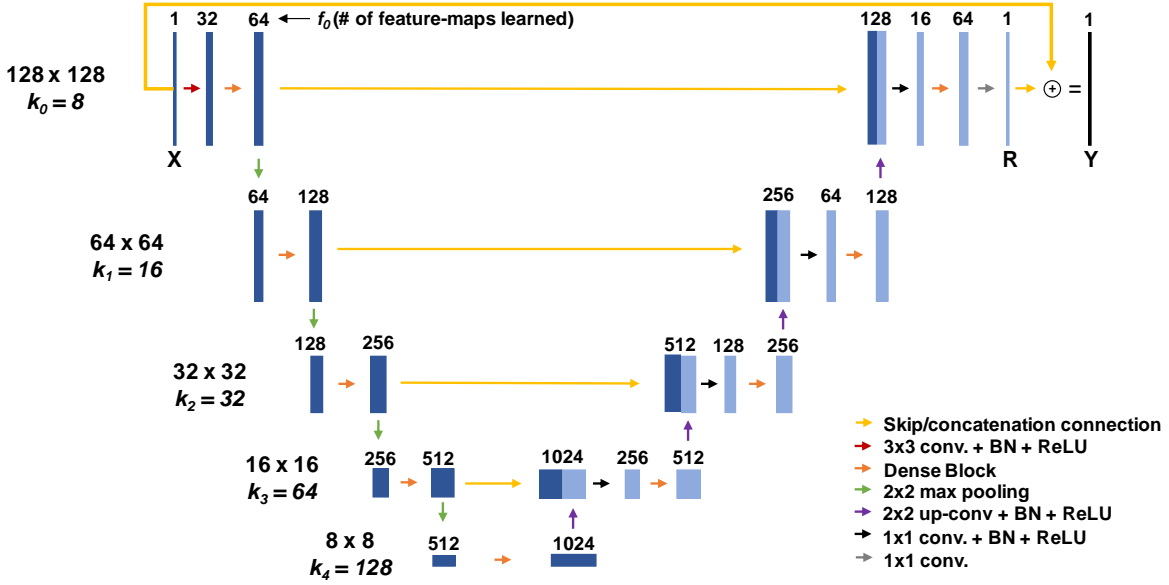


Fig. 3. Proposed FD-UNet architecture that incorporates dense connectivity [26] into the expanding and contracting path of the U-Net [19]. Hyperparameters for the illustrated architecture are $k_0 = 8$ and $f_0 = 64$ for an input image X of size 128×128 pixels.

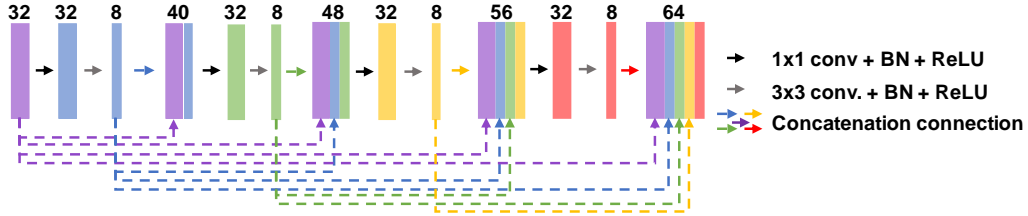


Fig. 4. Four layered dense block with a growth rate of $k_0 = 8$ and $F = 32$. Feature-maps learned in previous layers are concatenated with subsequent layers to learn the desired $f = 64$ feature-maps.

upsampling. Before each dense block in the upsampling process, the concatenated $2f$ feature-maps are reduced to $f/2$ using a 1×1 convolution.

In a dense block, earlier convolutional layers are connected to all subsequent layers via channel-wise concatenation [29], [30]. The ℓ^{th} layer's output have k feature-maps while its input have $F + k \times (\ell - 1)$ feature-maps, where F is the number of feature-maps in the input, as seen in Fig. 4. The hyperparameter k is the growth rate and regulates the number of feature-maps learned at each layer. To improve computational efficiency, a 1×1 convolution is applied prior to each 3×3 convolution reducing the number of feature-maps in the input to $4k$. The final output of the dense block is the concatenation between the input and the outputs of the ℓ layers.

The proposed CNN architecture utilizes residual learning by adding a skip connection between the input and output [35], [36]. In residual learning, the CNN learns to map the input image X to a residual image $R = Y - X$ and then recovers the target artifact-free image Y by adding the residual R to the input X . Residual learning is shown to mitigate the vanishing gradient problem. It is easier for the CNN to learn from the residual R because it often has a simpler structure than the original image.[25].

C. Synthetic Data for Training and Testing

Synthetic training and testing data is created using k-Wave, a MATLAB toolbox for simulating photoacoustic wave fields [37]. For each dataset, an initial photoacoustic source with a grid size of 128×128 is defined. Built-in functions of k-Wave are used to simulate the sparse measurement of the acoustic pressure and reconstruct an image containing artifacts using TR. The medium is assumed to be homogenous with a speed of sound of 1500 m/s and non-absorbing. Datasets are generated using three different synthetic phantoms and an experimentally-derived phantom created from an experimental dataset of mouse brain vasculature acquired using micro-CT. Although the brain vasculature is not acquired using PAT, the micro-CT images are used as an initial photoacoustic pressure source in k-Wave to create simulated PAT images of mouse brain vasculature.

The circles dataset is comprised of simple phantoms containing a variable number of circles up to a maximum of five, in which each circle has the same amplitude but has a center and radius chosen randomly from a uniform distribution [24]. Three different circle phantom datasets are generated using 15, 30, and 45 sensors. Each training and testing dataset respectively have $N = 1000$ and 200 images.

The Shepp-Logan phantom dataset is created by repeatedly applying transformations (scaling, rotation, and translation) to an initial image of the phantom. This data augmentation

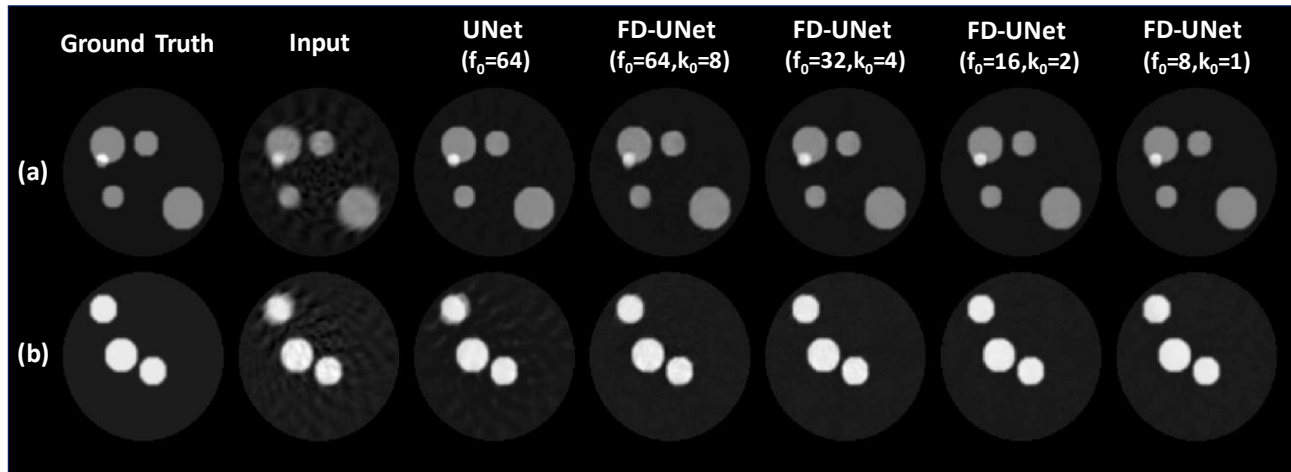


Fig. 5. Reconstructed circles images using TR, UNet, and FD-UNet with varying hyperparameters. (a) both CNNs recover a near artifact-free image. (b) example of the UNet reconstruction with residual background artifacts and the top-left circle has a distorted boundary.

strategy enables for many training and testing images with similar but also different image features to be generated [38]. The same strategy is also used to create the vasculature phantom dataset. For both phantom datasets, a testing dataset comprised of $N = 200$ images are generated. For the fine-tuning experiment, a fine-tuning dataset of $N = 100$ images are generated. The Shepp-Logan and vasculature phantom datasets are simulated in k-Wave using 30 sensors.

The experimentally derived mouse brain vasculature testing dataset is comprised of $N = 34$ maximum intensity projection images (MIPs) from 0.8 mm thick slices of a 3D volume acquired using micro-CT [39]. There is no training or fine-tuning dataset created from the experimentally derived mouse brain vasculature phantom. Instead, the CNN correcting artifacts in the experimentally derived testing dataset is trained on $N = 2000$ images of the circles and vasculature phantoms. Both the training and testing datasets are simulated in k-Wave using 30 sensors.

D. Deep Learning Implementation

The CNNs are implemented in Python 3.6 with TensorFlow v1.7, an open source deep learning software library [40]. Training and evaluation of the network is performed on a GTX 1080Ti NVIDIA GPU. The mean squared error is used as the loss function for training. The primary difference between the UNet and FD-UNet implementations is the inclusion of dense connectivity. The UNet learns the desired number of features using two consecutive 3×3 convolutional layer instead of through a dense block [24], [33].

III. EXPERIMENTS AND RESULTS

The UNet and FD-UNet are compared over several experiments to determine if dense connectivity enables for more artifacts to be removed and hence an image with higher quality to be recovered. For each experiment, both CNNs are trained for 10,000 iterations with a batch size of three images.

In the first experiment, the CNNs are used to remove artifacts from the circles phantom training dataset. Impact of CNN model complexity on image quality is explored by decreasing the hyperparameters, initial feature-maps learned (f_0) and

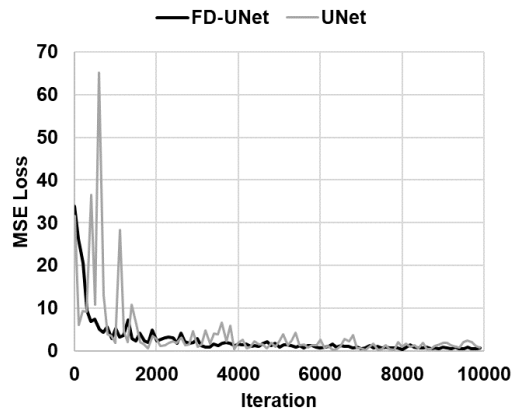


Fig. 6. MSE Loss during training for the FD-UNet ($f=64$, $k=8$) and UNet ($f=64$) on the circles training dataset ($N=30$ sensors).

TABLE I
AVERAGE PSNR AND NUMBER OF TRAINED PARAMETERS
FOR 2D CIRCLES DATASET (30 SENSORS)

	$f_0 = 8,$ $k_0 = 1$	$f_0 = 16,$ $k_0 = 2$	$f_0 = 32,$ $k_0 = 4$	$f_0 = 64,$ $k_0 = 8$
TR	32.48 ± 3.37			
UNet	33.56 ± 4.56 (487K)	34.85 ± 4.22 (1.9M)	34.96 ± 4.50 (7.8M)	35.10 ± 4.46 (31M)
FD-UNet	39.34 ± 3.03 (151K)	41.77 ± 3.38 (600K)	42.82 ± 3.20 (2.4M)	43.97 ± 3.28 (9.4M)

f_0 and k_0 are CNN hyperparameters. k_0 is only applicable to the FD-UNet. Number of trained parameters for each CNN are shown in parenthesis.

dense block growth rate (k_0). Furthermore, the CNNs are used to correct images with increasingly severe sparse sampling artifacts to determine the extent of artifact severity that can be removed by each CNN.

In the second experiment, the CNNs are used to remove artifacts from the Shepp-Logan and vasculature phantom datasets. They are both initially trained on the circles dataset and used to remove artifacts from the Shepp-Logan and vasculature phantom testing datasets. The trained CNNs are then fine-tuned by additionally training each CNN on each

respective smaller phantom fine-tuning dataset for 5,000 iterations. The purpose of this experiment is to determine how well each CNN performs and generalizes when the training and testing datasets are not well-matched (e.g. training on circles but testing on vasculature). The fine-tuning experiment demonstrates whether it is feasible to predominantly train a CNN on an unmatched dataset and then fine-tune on a smaller matched dataset. The CNNs are not trained from scratch on full datasets of the Shepp-Logan and vasculature phantom because Antholzer et al has shown previously that appropriately matching the training and testing data generally leads to a CNN with good performance.

In the third experiment, the CNNs are tested on correcting artifacts of the experimentally-derived mouse brain vasculature testing dataset. The CNNs are trained on a dataset comprised of the circles and vasculature phantom images without any additional fine-tuning. Similar to the previous experiment, the intent is to determine how well the CNNs perform when trained on mismatched data. However, in this scenario, the CNNs are trained only on images of synthetic phantoms but are tested on images of an experimentally derived phantom that likely contain image features not observed in the training data. Image reconstruction quality is quantified using the peak signal-to-noise ratio (PSNR) between the ground truth and reconstructed image. For each experiment, the average PSNR of the testing dataset and standard deviation is reported.

A. Circles Dataset

Fig. 5. and Table 1 compare the image quality between the UNet and FD-UNet for the circles dataset. Undersampling artifacts are observed in the initial images reconstructed with TR. Both CNNs typically recover a near artifact-free image, but there are instances where the FD-UNet succeeds while the UNet fails. There are no instances of the reverse observed in the testing dataset. As seen in the UNet reconstruction of Fig. 5b., there are residual background artifacts remaining and the top-left circle has a distorted boundary. The FD-UNet reconstruction has no background artifacts and the circle is correctly reconstructed.

The FD-UNet significantly outperforms the UNet as summarized in Table 1. The FD-UNet has a higher average PSNR with a lower standard deviation indicating better image quality and more robust performance. The FD-UNet also requires far fewer parameters than the UNet to achieve better performance. Interestingly, the most compact FD-UNet ($f = 8$, $k = 1$) outperforms the best performing UNet ($f = 64$). As the total number of features learned is increased, the FD-UNet benefits more from the increased model complexity. Both CNNs converge to an approximate minimum loss by 4,000 training steps, as seen in Fig. 6. However, the UNet loss appears to be more volatile when compared to the FD-UNet loss.

Fig. 7 and Table 2 show image reconstructions of the circles dataset under different levels of sampling sparsity. In this experiment, the trained CNNs are only tested on a matching dataset created using the same number of sensors. Difference between the CNNs' performance is clearly seen in Fig. 7a, where the overlapping circles in the UNet reconstruction are blurred together while they can be distinguished in the FD-UNet reconstruction.

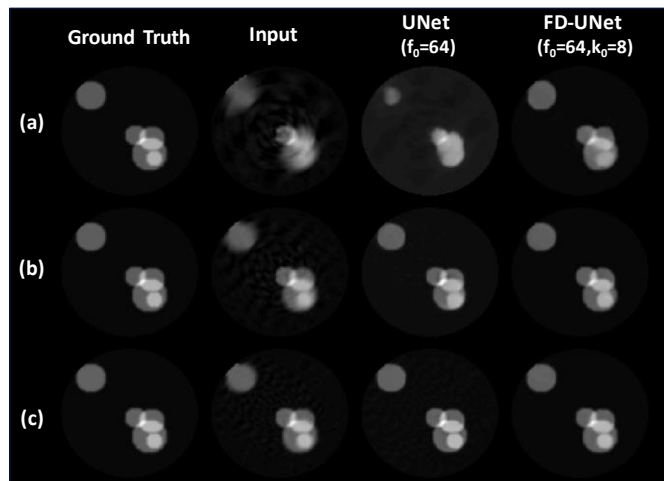


Fig. 7. Reconstructed circles images under different levels of sampling sparsity using (a) 15 sensors, (b) 30 sensors, and (c) 45 sensors.

TABLE II
AVERAGE PSNR UNDER VARYING SAMPLING SPARSITY LEVELS

# of Sensors	$N = 15$	$N = 30$	$N = 45$
TR	27.22 ± 2.99	32.48 ± 3.37	36.11 ± 3.37
UNet ($f_0 = 64$)	27.51 ± 3.88	35.10 ± 4.46	39.80 ± 4.42
FD-UNet ($f_0 = 64, k_0 = 8$)	38.44 ± 4.51	43.97 ± 3.28	46.60 ± 1.89

B. Shepp-Logan and Vasculature Phantom Dataset

Fig. 8. and Table 3 show reconstructions of the Shepp-Logan and vasculature phantoms for both CNNs with and without fine tuning. The CNNs are initially trained on the only circles dataset and both recover a good albeit blurred reconstruction of the Shepp-Logan phantom, as seen in Fig. 8a. While the undersampling artifacts are removed, the reconstructed images have a lower PSNR compared to TR. However, both CNNs with fine-tuning recover a near artifact free image with an improved PSNR.

Both CNNs without fine-tuning recover an image of the vasculature phantom with circular-like features that has a lower PSNR compared to the TR reconstruction. As seen in Fig. 8b, the FD-UNet does typically remove more of the background artifacts. Both CNNs with fine-tuning recover a sharper near artifact free image. For both phantom datasets, the FD-UNet outperforms the UNet and recovers a reconstruction with a higher average PSNR.

C. Experimentally Derived Mouse Brain Vasculature Dataset

In this experiment, the CNNs are only trained on images of the circles and vasculature phantom and not fine-tuned any micro-CT MIPs. Fig. 9. show reconstructions of experimentally acquired micro-CT MIPs of mouse brain vasculature. The FD-UNet corrects most background artifacts and recovers many of the larger vessels. There are instances in which residual background artifacts remain in the UNet reconstruction as seen in Fig. 9a. Many of the smaller details are lost in both the TR and CNN reconstructions. There is a small improvement in the average PSNR of the UNet (27.08 ± 1.22) and FD-UNet

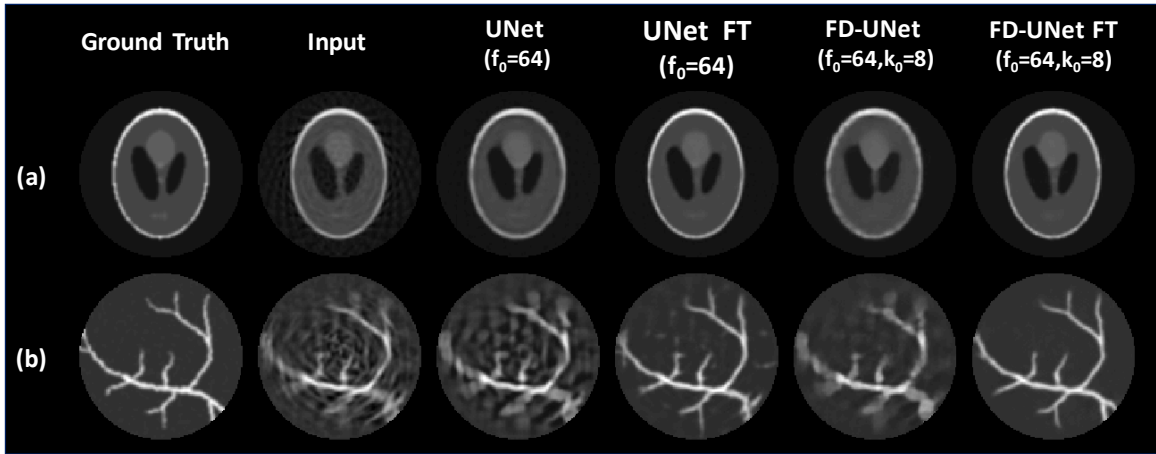


Fig. 8. Reconstructed images (30 sensors) of the (a) Shepp-Logan phantom and (b) vasculature phantom with and without fine-tuning (FT).

(27.43 ± 1.11) over the TR reconstructions (26.88 ± 1.10). Differential overlays between the reconstruction and the ground truth image reveal that artifacts affect the entire image and obscure small details in the TR reconstruction. Whereas, differences due to artifacts or missing details are typically localized to the location of vessels in the CNN reconstructions.

IV. DISCUSSION

In this work, we propose a novel CNN architecture termed FD-UNet that builds upon the deep learning framework by Antholzer et al. for removing artifacts from 2D PAT images reconstructed from sparse data. By incorporating dense connectivity, the FD-UNet requires fewer parameters and recovers images with a higher quality than the UNet.

The FD-UNet consistently outperforms the UNet in removing artifacts for the circles phantom dataset while requiring fewer parameters as summarized in Table 1. The improved performance is likely due to the dense connectivity pattern mitigating the problem of overfitting and encouraging the CNN to learn a more diverse set of features [29]. As seen in Fig. 6., the UNet loss is much more volatile than the FD-UNet loss, which indicates that the UNet is likely overfitting to the training data. This issue is illustrated in Fig. 8b., in which both CNNs are trained on the circles dataset, but the FD-UNet learns a set of features that generalizes better and is able to remove more of the background artifacts.

In addition to mitigating overfitting, dense connectivity improves information flow and promotes feature reuse throughout the network. This advantage can be seen in Fig. 5., where the most compact FD-UNet ($f_0 = 8, k_0 = 1$) achieves a higher average PSNR than the best performing UNet ($f_0 = 64$). Despite the FD-UNet having less model complexity and representational power, it is able to effectively learn a set of features that allows for high quality reconstructions. Furthermore, the FD-UNet uses only about a hundredth of the parameters compared to the UNet. Having a more compact CNN with fewer parameters requires less computation and hence faster image reconstruction.

Reducing the number of sensors leads to increasingly more severe artifacts in the TR reconstruction as seen in Fig. 7. There is a limit to how few sensors can be used because information

TABLE III
AVERAGE PSNR FOR SHEPP-LOGAN AND VASCULATURE PHANTOM DATASET (30 SENSORS)

	Shepp-Logan		Vasculature	
	Initial	Fine-tuned	Initial	Fine-tuned
TR	32.50 ± 1.53		24.79 ± 2.86	
UNet	31.69 ± 1.19	36.23 ± 2.46	24.40 ± 2.93	25.96 ± 2.85
FD-UNet	30.81 ± 0.97	38.24 ± 1.69	25.27 ± 2.16	31.30 ± 2.24

is lost as a result of sparse sampling. The CNNs are likely reducing the artifacts by a combination of recovering lost information based on the artifact patterns observed and adding information learned from the training data. For example, the FD-UNet is able to recover a good reconstruction of the circles phantom when the number of sensors is reduced to 15, but it is not clear whether it would perform as well with more complex images.

A potential drawback of a CNN based approach is that its performance is heavily tied to the training data provided. In particular, the image features between the training and testing datasets needs to be sufficiently similar. This necessity is demonstrated by the fact that both CNNs recover good reconstructions of the Shepp-Logan phantom since the phantom and circles training data are similar. The CNNs incorrectly reconstruct the vasculature phantom with circular-like features as a result of only training on the circles dataset. However, only a small dataset of vasculature images is needed for fine-tuning the CNN to recover good reconstructions. The results provide evidence that it may be feasible to train a to predominantly train a CNN on an unmatched dataset and then fine-tune on a smaller matched dataset.

In the third experiment, the FD-UNet is trained on images of the circles and vasculature phantom but used to correct artifacts in the experimentally derived mouse brain vasculature dataset as seen in Fig. 9. Despite having not trained on any mouse brain vasculature images, the FD-UNet reliably reconstructs most larger vessels and corrects majority of the background artifacts. While these larger structures are clearly more visible in the FD-UNet reconstruction, there is only a small improvement in the average PSNR because many of the smaller vessels are missing.

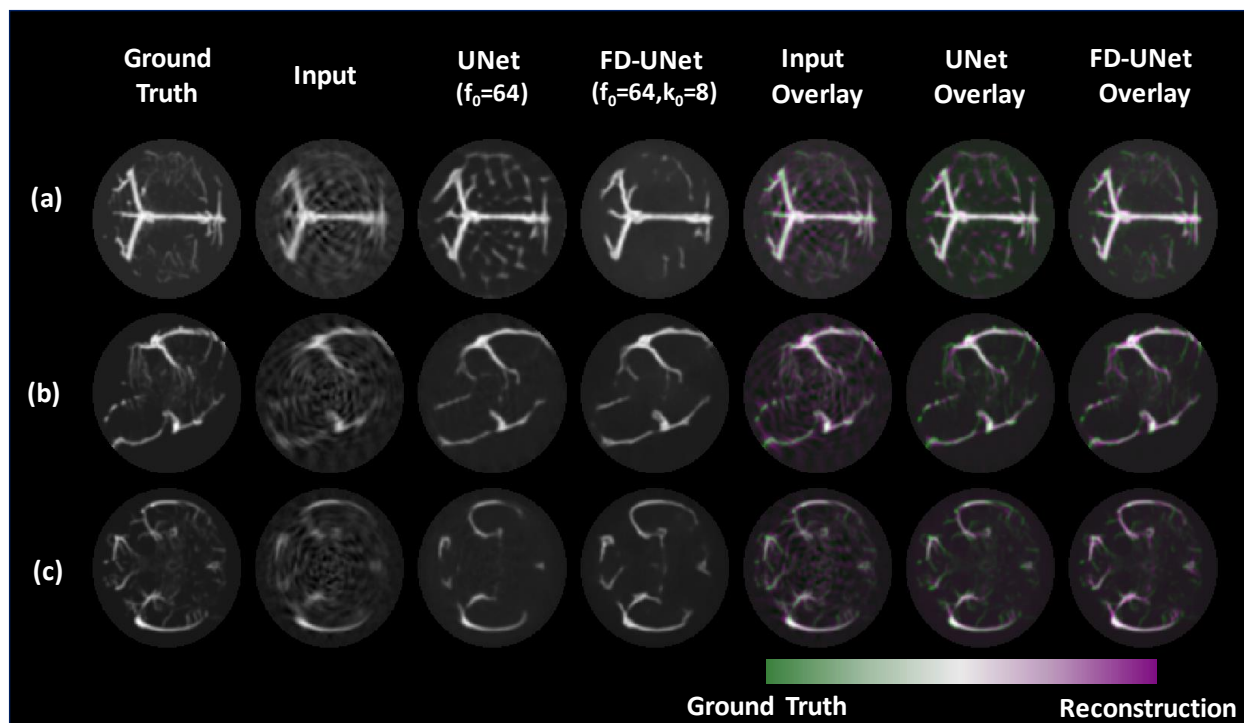


Fig. 9. Reconstructed images of micro-CT mouse brain vasculature MIPs. Reconstructed images are overlaid with the ground truth to visualize reconstruction errors. Features that are missing in the FD-UNET images but present in the ground truth images are shown in green. Artifacts introduced by TR that were persistent despite the use of FD-UNET are shown in magenta.

This highlights a limitation of the post-processing based deep learning framework. Features such as small vessels that are severely obscured by artifacts and cannot be observed in the initial TR reconstruction also likely cannot be reconstructed by the CNN. In that scenario, much of the information required to recover small vessels is lost as a result of sparse sampling. It might be possible to reconstruct some of the smaller vessels if the CNN is used to directly reconstruct the measured pressure data into an image. There may be some useful information in the measured pressure data that is lost during the TR reconstruction. Otherwise, additional sensors would be needed to sample the data to recover the finer details.

V. CONCLUSION

In this paper, we propose a novel CNN architecture termed FD-UNet for removing artifacts from 2D PAT images reconstructed from sparse data. We compare the performance between the FD-UNet and the UNet on simulated datasets based on a simple circles, Shepp-Logan, and vasculature phantoms. For all experiments, the FD-UNet requires far fewer parameters and recover higher quality reconstructions. Furthermore, we demonstrate the feasibility of training the FD-UNet on synthetic phantoms for removing artifacts in experimentally derived mouse brain vasculature images.

REFERENCES

- [1] R. A. Kruger, P. Liu, Y. “Richard” Fang, and C. R. Appledorn, “Photoacoustic ultrasound (PAUS)—Reconstruction tomography,” *Med. Phys.*, vol. 22, no. 10, pp. 1605–1609, Oct. 1995.
- [2] P. Beard, “Biomedical photoacoustic imaging,” *Interface Focus*, vol. 1, no. 4, pp. 602–631, Aug. 2011.
- [3] J. Xia, J. Yao, and L. V. Wang, “Photoacoustic tomography: principles and advances,” *Electromagn. Waves Camb. Mass*, vol. 147, pp. 1–22, 2014.
- [4] V. Ntziachristos, J. Ripoll, L. V. Wang, and R. Weissleder, “Looking and listening to light: the evolution of whole-body photonic imaging,” *Nat. Biotechnol.*, vol. 23, no. 3, pp. 313–320, Mar. 2005.
- [5] J. Yao and L. V. Wang, “Photoacoustic tomography: fundamentals, advances and prospects,” *Contrast Media Mol. Imaging*, vol. 6, no. 5, pp. 332–345, Sep. 2011.
- [6] M. Xu and L. V. Wang, “Universal back-projection algorithm for photoacoustic computed tomography,” presented at the Photons Plus Ultrasound: Imaging and Sensing 2005: The Sixth Conference on Biomedical Thermoacoustics, Optoacoustics, and Acousto-optics, 2005, vol. 5697, pp. 251–255.
- [7] M. Haltmeier, O. Scherzer, and G. Zangerl, “A reconstruction algorithm for photoacoustic imaging based on the nonuniform FFT,” *IEEE Trans. Med. Imaging*, vol. 28, no. 11, pp. 1727–1735, Nov. 2009.
- [8] K. Wang and M. A. Anastasio, “A simple Fourier transform-based reconstruction formula for photoacoustic computed tomography with a circular or spherical measurement geometry,” *Phys. Med. Biol.*, vol. 57, no. 23, pp. N493–N499, Dec. 2012.
- [9] P. Burgholzer, G. J. Matt, M. Haltmeier, and G. Paltauf, “Exact and approximative imaging methods for photoacoustic tomography using an arbitrary detection surface,” *Phys. Rev. E Stat. Nonlin. Soft Matter Phys.*, vol. 75, no. 4 Pt 2, p. 046706, Apr. 2007.
- [10] B. E. Treeby, E. Z. Zhang, and B. T. Cox, “Photoacoustic tomography in absorbing acoustic media using time reversal,” *Inverse Probl.*, vol. 26, no. 11, p. 115003, 2010.
- [11] B. T. Cox and B. E. Treeby, “Artifact Trapping During Time Reversal Photoacoustic Imaging for Acoustically Heterogeneous Media,” *IEEE Trans. Med. Imaging*, vol. 29, no. 2, pp. 387–396, Feb. 2010.
- [12] Y. Hristova, P. Kuchment, and L. Nguyen, “Reconstruction and time reversal in thermoacoustic tomography in acoustically homogeneous

- and inhomogeneous media,” *Inverse Probl.*, vol. 24, no. 5, p. 055006, 2008.
- [13] M. Haltmeier, “Sampling Conditions for the Circular Radon Transform,” *IEEE Trans. Image Process.*, vol. 25, no. 6, pp. 2910–2919, Jun. 2016.
- [14] A. Rosenthal, V. Ntziachristos, and D. Razansky, “Acoustic Inversion in Optoacoustic Tomography: A Review,” *Curr. Med. Imaging Rev.*, vol. 9, no. 4, pp. 318–336, Nov. 2013.
- [15] S. Arridge *et al.*, “Accelerated high-resolution photoacoustic tomography via compressed sensing,” *Phys. Med. Biol.*, vol. 61, no. 24, p. 8908, 2016.
- [16] J. Friel and M. Haltmeier, “Efficient regularization with wavelet sparsity constraints in PAT,” *ArXiv170308240 Math*, Mar. 2017.
- [17] C. Huang, K. Wang, L. Nie, L. V. Wang, and M. A. Anastasio, “Full-Wave Iterative Image Reconstruction in Photoacoustic Tomography With Acoustically Inhomogeneous Media,” *IEEE Trans. Med. Imaging*, vol. 32, no. 6, pp. 1097–1110, Jun. 2013.
- [18] K. Wang, R. Su, A. A. Oraevsky, and M. A. Anastasio, “Investigation of iterative image reconstruction in three-dimensional optoacoustic tomography,” *Phys. Med. Biol.*, vol. 57, no. 17, p. 5399, 2012.
- [19] Y. LeCun, Y. Bengio, and G. Hinton, “Deep learning,” *Nature*, vol. 521, no. 7553, pp. 436–444, May 2015.
- [20] O. Ronneberger, P. Fischer, and T. Brox, “U-Net: Convolutional Networks for Biomedical Image Segmentation,” *ArXiv150504597 Cs*, May 2015.
- [21] Ö. Çiçek, A. Abdulkadir, S. S. Lienkamp, T. Brox, and O. Ronneberger, “3D U-Net: Learning Dense Volumetric Segmentation from Sparse Annotation,” *ArXiv160606650 Cs*, Jun. 2016.
- [22] A. Esteva *et al.*, “Dermatologist-level classification of skin cancer with deep neural networks,” *Nature*, vol. 542, p. 115, Jan. 2017.
- [23] R. Fakoor, F. Ladhak, A. Nazi, and M. Huber, “Using deep learning to enhance cancer diagnosis and classification,” p. 7.
- [24] S. Antholzer, M. Haltmeier, and J. Schwab, “Deep Learning for Photoacoustic Tomography from Sparse Data,” *ArXiv170404587 Cs*, Apr. 2017.
- [25] Y. S. Han, J. Yoo, and J. C. Ye, “Deep Residual Learning for Compressed Sensing CT Reconstruction via Persistent Homology Analysis,” *ArXiv161106391 Cs*, Nov. 2016.
- [26] K. H. Jin, M. T. McCann, E. Froustey, and M. Unser, “Deep Convolutional Neural Network for Inverse Problems in Imaging,” *IEEE Trans. Image Process.*, vol. 26, no. 9, pp. 4509–4522, Sep. 2017.
- [27] S. Antholzer, M. Haltmeier, R. Nuster, and J. Schwab, “Photoacoustic image reconstruction via deep learning,” in *Photons Plus Ultrasound: Imaging and Sensing 2018*, 2018, vol. 10494, p. 104944U.
- [28] A. Hauptmann *et al.*, “Model based learning for accelerated, limited-view 3D photoacoustic tomography,” *ArXiv170809832 Cs Math*, Aug. 2017.
- [29] G. Huang, Z. Liu, L. van der Maaten, and K. Q. Weinberger, “Densely Connected Convolutional Networks,” *ArXiv160806993 Cs*, Aug. 2016.
- [30] X. Li, H. Chen, X. Qi, Q. Dou, C.-W. Fu, and P. A. Heng, “H-DenseUNet: Hybrid Densely Connected UNet for Liver and Liver Tumor Segmentation from CT Volumes,” *ArXiv170907330 Cs*, Sep. 2017.
- [31] S. Ioffe and C. Szegedy, “Batch Normalization: Accelerating Deep Network Training by Reducing Internal Covariate Shift,” *ArXiv150203167 Cs*, Feb. 2015.
- [32] S. Santurkar, D. Tsipras, A. Ilyas, and A. Madry, “How Does Batch Normalization Help Optimization? (No, It Is Not About Internal Covariate Shift),” *ArXiv180511604 Cs Stat*, May 2018.
- [33] J. Long, E. Shelhamer, and T. Darrell, “Fully Convolutional Networks for Semantic Segmentation,” *ArXiv14114038 Cs*, Nov. 2014.
- [34] A. Krizhevsky, I. Sutskever, and G. E. Hinton, “ImageNet Classification with Deep Convolutional Neural Networks,” in *Advances in Neural Information Processing Systems 25*, F. Pereira, C. J. C. Burges, L. Bottou, and K. Q. Weinberger, Eds. Curran Associates, Inc., 2012, pp. 1097–1105.
- [35] J. Kim, J. K. Lee, and K. M. Lee, “Accurate Image Super-Resolution Using Very Deep Convolutional Networks,” *ArXiv151104587 Cs*, Nov. 2015.
- [36] K. He, X. Zhang, S. Ren, and J. Sun, “Deep Residual Learning for Image Recognition,” *ArXiv151203385 Cs*, Dec. 2015.
- [37] B. E. Treeby and B. T. Cox, “k-Wave: MATLAB toolbox for the simulation and reconstruction of photoacoustic wave fields,” *J. Biomed. Opt.*, vol. 15, no. 2, p. 021314, Apr. 2010.
- [38] “- k-Wave MATLAB Toolbox.” [Online]. Available: http://www.k-wave.org/documentation/example_pr_2D_tr_circular_sensor.php. [Accessed: 25-Jun-2018].
- [39] A. Dorr, J. G. Sled, and N. Kabani, “Three-dimensional cerebral vasculature of the CBA mouse brain: a magnetic resonance imaging and micro computed tomography study,” *NeuroImage*, vol. 35, no. 4, pp. 1409–1423, May 2007.
- [40] M. Abadi *et al.*, “TensorFlow: Large-Scale Machine Learning on Heterogeneous Distributed Systems,” p. 19.